Microstructural control of TiC/a-C nanocomposite coatings with pulsed magnetron sputtering

Pei, Y.T.; Chen, C.Q.; Shaha, K.P.; Hosson, J.Th.M. De; Bradley, J.W.; Voronin, S.A.; Čada, M.

Published in:
Acta Materialia

DOI:
10.1016/j.actamat.2007.10.025

Available online at www.sciencedirect.com
ScienceDirect
Acta Materialia 56 (2008) 696–709
Acta MATERIALIA
www.elsevier.com/locate/actamat

Microstructural control of TiC/a-C nanocomposite coatings with pulsed magnetron sputtering

Y.T. Pei [a], C.Q. Chen [a], K.P. Shaha [a], J.Th.M. De Hosson [a,*], J.W. Bradley [b], S.A. Voronin [b], M. Čada [b]

[a] Department of Applied Physics, The Netherlands Institute for Metals Research, University of Groningen, Nijenborgh 4, 9747 AG Groningen, The Netherlands
[b] Department of Electrical Engineering and Electronics, University of Liverpool, Brownlow Hill, Liverpool L69 3GJ, UK

Received 13 April 2007; received in revised form 9 October 2007; accepted 10 October 2007
Available online 3 December 2007

Abstract

In this paper, we report some striking results on the microstructural control of TiC/a-C nanocomposite coatings with pulsed direct current (DC) magnetron sputtering. The interface morphology and microstructure evolution as a function of pulse frequency and duty cycle were scrutinized using atomic force microscopy, scanning electron microscopy and high-resolution transmission electron microscopy techniques. It is shown that, with increasing pulse frequency, the nanocomposite coatings exhibit evolutions in morphology of the growing interface from rough to smooth and in the microstructure from strongly columnar to fully columnar-free. In addition, the smoothly growing interface favors the formation of a tailor-made multilayered nanocomposite structure. The fundamental mechanisms are analyzed with the assistance of plasma diagnostic experiments. Ion mass/energy spectrometry measurements reveal that, depending on the frequency and duty cycle of DC pulses, pulsing of the magnetrons can control the flux and energy distribution of Ar^+ ions over a very broad range for concurrent impingement on the growing interface of deposited coatings, in comparison with DC sputtering. The significantly enhanced energy flux density is thought to be responsible for the "adatom transfer" in interface smoothening and thus the restraint of columnar growth.

Keywords: Thin film; Magnetron sputtering; Nanostructure; Interface smoothening; Growth behavior

1. Introduction

Pulsed direct current (p-DC) magnetron sputtering in combination with an unbalanced magnetron configuration has become a major technique in the deposition of advanced coatings during the last decade [1–3]. It has the significant advantage over DC magnetron sputtering in suppressing arcing at the targets during reactive sputtering and in sputtering non-conductive materials. In particular, it may improve the microstructure and properties of deposited coatings, which strongly depend on the intensity of the concurrent ion impingement on the growing interface. The crucial parameters determining the intensity of ion impingement are the energy distribution of the impinging ions and the flux ratio between the impinging ions and the depositing atoms. It has been observed that pulsing magnetrons in the mid frequency regime (up to 350 kHz) leads to a greatly extended energy distribution of impinging ions and a higher ion current density towards the substrate [4,5]. As a result, dense, well-structured coatings can be grown in pulsed mode [6,7]. However, contradictory results are also reported that substrate heating rate decreases with increasing frequency of p-DC sputtering, implying a reduced energy being transferred to the growing film [8]. A thorough understanding of the mechanisms of plasma control and microstructure manipulation using pulsed DC magnetron sputtering is still in development, but it will

* Corresponding author. Tel.: +31 50 363 4898; fax: +31 50 363 4881.
E-mail address: j.t.m.de.hosson@rug.nl (J.Th.M. De Hosson).

1359-6454/$30.00 © 2007 Acta Materialia Inc. Published by Elsevier Ltd. All rights reserved.
doi:10.1016/j.actamat.2007.10.025

most certainly lead to its strength as a production technique for advanced coatings being promoted.

Recent work on plasma diagnostics of p-DC magnetron sputtering has revealed that pulsing the magnetrons may modify the intrinsic plasma parameters to deliver higher ion flux and energy to the growing films. Electric probe measurements have demonstrated higher plasma densities and electron temperature adjacent to the substrate [9,10]. These are the primary causes for the generation of higher ion energy and flux to the growing films. Time-averaged mass spectrometry measurements at the substrate position have proved the presence of a significant fraction of the high energy ions and middle energy ions in pulsed magnetron sputtering [4]. These two groups of ions are generated at the high positive overshot during the transition phase and the low positive voltage in the reverse phase, respectively, in the bipolar pulse mode. A few models and simulations have been proposed to explain the gain in the ion flux and energy, and its temporal evolution during the pulse transition and off time [10–12]. Lin et al. [13] systematically studied the time-averaged energy spectra of the positive ions during p-DC reactive sputtering of Cr and Al targets in an argon and nitrogen mixture with respect to the effects of pulsed power, working pressure, nitrogen-to-argon flow ratio, substrate-to-chamber wall distance and different pulsing parameters under synchronized and asynchronized conditions. It has been shown that both the pulsing parameters and other deposition parameters affect the ion energies and fluxes drawn to the substrate. However, the deposition parameters hardly influence the characteristic ion energy distribution of p-DC magnetron sputtering, namely the three groups of ion population, in a wide energy range.

Different coatings have been deposited via p-DC magnetron sputtering and improved microstructure or/and enhanced properties have been reported [13–15], which were attributed to the intensified concurrent ion impingement. Apparently, the mechanisms of enhancement may be rather different from one coating system to another, and this needs to be scrutinized with advanced microscopy on different length scales. However, care should be taken in inspecting micrographs because the effects of p-DC magnetron sputtering on the growth behavior and microstructure of deposited coatings may be hidden. For instance, an inappropriately fractured cross-section of coatings with a strong columnar characteristic, exhibited by non-flatness or an "S"-shaped profile along the thickness direction, might appear "column-free". On the other hand, fracture patterns on an inappropriately fractured cross-section of column-free coatings were interpreted as columnar boundaries.

Our recent work has shown that the columnar boundaries (CBs) of TiC/a-C:H nanocomposite coatings are a potential source of failure under loading and contact sliding [16,17]. The CBs may act as initiation sites for cracks and preferential cracking paths, attributed to the fact that the homogeneity of a nanocomposite is interrupted by the CBs, which are enriched in carbon and voids. The columnar boundaries originate from the deep groove networks formed on the growing interfaces. In reactive sputtering, the CBs can be readily restrained by employing higher voltage substrate bias or increasing the flow rate of hydrocarbon gas. The mechanisms of column restraint involved in manipulating these two parameters are different, i.e. breaking down the groove structure through intensive ion impingement or filling in the grooves with carbon adatoms of high mobility, respectively [18]. However, manipulating bias voltage and carbon content is not efficient enough to restrain the columnar growth in DC non-reactive sputtering of TiC/a-C nanocomposite coatings, where the flux density of sputtered atoms reaching the substrate surface and ion impingement may fluctuate to a large extent when the substrates pass from one target to another. The purpose of this work is to study the effects of pulsed DC sputtering on the deposition process and microstructure evolution of TiC/a-C nanocomposite coatings, in particular on the restraint of column growth. With increasing pulse frequency, the growing interface evolves from rough cauliflower patterns to atomically smooth. Physical arguments are proposed to understand this interface evolution. Further detailed characterization of the nanostructure and properties of deposited TiC/a-C nanocomposite coatings will be published elsewhere.

2. Experiments

TiC/a-C nanocomposite coatings were deposited with non-reactive sputtering in a TEER UDP400/4 closed-field unbalanced magnetron sputtering system. The system was configured of one Ti target (99.7%), one Cr target (99.5%) and two graphite targets (99.99%) opposite each other. The size of all the targets was $200 \times 100\ mm^2$. The two magnetrons with a metallic target were powered by a Pinnacle 6/6 kW double channel DC power supply (Advanced Energy) and the other two magnetrons with graphite targets were powered by a Pinnacle Plus 5/5 kW double channel p-DC power supply (Advanced Energy). The substrates were biased by a Pinnacle Plus 5 kW single channel p-DC power supply (Advanced Energy). All the power supplies for sputtering were operated at current regulation mode via a computer-controlled system. The UDP 400/4 system was installed with an oil-free pumping system (a turbo molecular pump plus a diaphragm backing pump).

The substrates used for each coating were $\varnothing 30 \times 6$ mm discs of hardened M2 steel for tribological tests and $\varnothing 50$ mm Si wafer for microscopic observation of coating fracture cross-sections and for residual stress measurements by monitoring the curvature change. Prior to deposition, the substrates were ultrasonically cleaned in acetone. The base pressure of the chamber before deposition was $3–4 \times 10^{-6}$ mbar, and the deposition pressure 2.66×10^{-3} mbar was reached with a constant flow of argon gas. The substrates were p-DC sputter-cleaned for 15 min at −400 V bias voltage, 250 kHz and 87.5% duty cycle. No

intended heating on the substrates was used during deposition. Nevertheless, the maximum temperature reached during deposition of each batch was measured on the sample holder. A 200 nm thick ductile CrTi interlayer of optimized composition and structure was employed to enhance the interfacial adhesion of TiC/a-C nanocomposite coatings. The interfacial adhesion was quantified by scratch tests with a CSM Revetester. The hardness and indentation modulus of the coatings were measured by nanoindentation with an MTS Nanoindenter XP®. The microstructural evolutions of the coatings were characterized with a Philips XL-30S FEG high-resolution scanning electron microscope on fracture cross-sections and a DI NanoScope IIIa atomic force microscope was used to image the surface morphology and to measure the surface roughness. The captured atomic force microscopy (AFM) micrographs were displayed and analyzed with free software WSxM® [19]. The nanostructure of the coatings was revealed by high-resolution transmission electron microscopy using a JEOL 2010-FEG microscope.

An EQP300 quadrupole mass spectrometer/ion energy analyser (Hiden Analytical Ltd.) was used to measure the energy distribution of impinging ions in a single unbalanced magnetron sputtering system, GENLAB (GENCOA Ltd.), installed with a ∅150 mm circular magnetron. It had a typical unbalanced configuration of adjustable magnetic field strength, which was set to resemble the field strength of the magnetrons installed in the TEER UDP400/4 rig. The single magnetron was powered with a 5 kW Pinnacle Plus unit and operated at sputtering parameters comparable to those used for coating deposition. The extractor head of the EQP300 instrument was pointed to the racetrack of the target and fixed directly behind a metallic substrate at the distance of 100 mm from the target, which had a large opening hole that was covered with a fine nickel grid and aligned with the entrance orifice (∅100 μm) of the extractor. For the detailed set-up, see Ref. [4]. The ion energies were effectively measured with reference to the ground potential of the chamber wall. The counts of Ar^+ ions in each energy bin $\langle E, E + dE\rangle$, where $dE = 0.1$ eV was the energy resolution of the instrument, were accumulated for a 10 ms time period and one scan of the whole energy spectra took 20 s. Therefore, the ion counts of different energies were a direct measure of the ion flux and can be confidently compared among the measurements, provided the instrument settings remained unchanged.

3. Results

3.1. DC magnetron sputtering of TiC/a-C nanocomposite coatings

In our recent work on the deposition of TiC/a-C:H nanocomposite coatings with reactive DC sputtering in an argon/acetylene atmosphere, it was revealed that the undesired columnar microstructure can be fully restrained by applying a higher substrate bias voltage (up to 150 V) and/or a higher flow rate of acetylene gas that corresponds to a maximum carbon content of 88 at.% (excluding hydrogen) [16]. The columnar growth is directly related to the interface structure of the growing coatings. Typically, cauliflower-like patterns characterize the surface topography of the nanocomposite coatings such that the cauliflower branches are separated by groove networks with a maximum depth of about 10 nm. These deep groove networks are the likely origin of the CBs, which is supported by the fact that the CBs intersect with the growing interfaces at the deep groove networks [18]. One can envisage that restraining the formation of groove networks will lead to the destruction of CBs and thus a column-free coating. In fact, the mechanisms involved in manipulating the two deposition parameters (bias voltage and flow rate of acetylene) are different. That is to say, the former breaks down the groove structure through intensive ion impingement and the latter directly fills the grooves with hydrocarbon adatoms of high mobility, respectively.

Following this approach, hydrogen-free TiC/a-C nanocomposite coatings were deposited by non-reactive magnetron sputtering graphite and titanium targets. Fig. 1 shows the microstructural evolution of DC sputtered TiC/a-C coatings of nearly the same composition with increasing substrate bias voltage. It is obvious that the columnar microstructure is always present in the coating, even though the columns become thicker and the coating gets denser with increasing bias voltage up to 80 V. Further increasing the bias voltage to 100 V makes the columnar character stronger and the coating less dense, due to the formation of facets on the head of growing columns and thus a much rougher interface of the growing coating. Finally, the coating deposited at 120 V bias voltage flakes off. There is no way to fully suppress the columnar microstructure of the TiC/a-C nanocomposite coatings by only increasing the substrate bias voltage under DC magnetron non-reactive sputtering. In addition, it is noteworthy that an increase in substrate bias voltage narrows the space suitable for depositing the coatings, in terms of the distance from targets. When applying a lower negative bias voltage (40 or 60 V), it is possible to deposit dense coatings at a distance of 100 mm from the targets although the deposition rate is lower than that at a distance of 70 mm (Fig. 1a and b). However, the coating deposited at the same distance of 100 mm becomes porous and less dense once the bias voltage is increased to 80 V. An even worse situation is seen at 100 V bias, where the coating deposited at 80 mm distance is already porous (Fig. 1d). In this case, only the coating deposited at 60 mm distance from the targets is fully dense but still with a columnar microstructure (not shown). Such a reduction of suitable space for deposition is attributed to the excess impingement of highly energetic but low flux ions, as to be discussed in the next section.

The next step in our study of DC sputtering deposition parameters was to vary the carbon content of the coatings and to check the effect on the restraint of columnar growth.

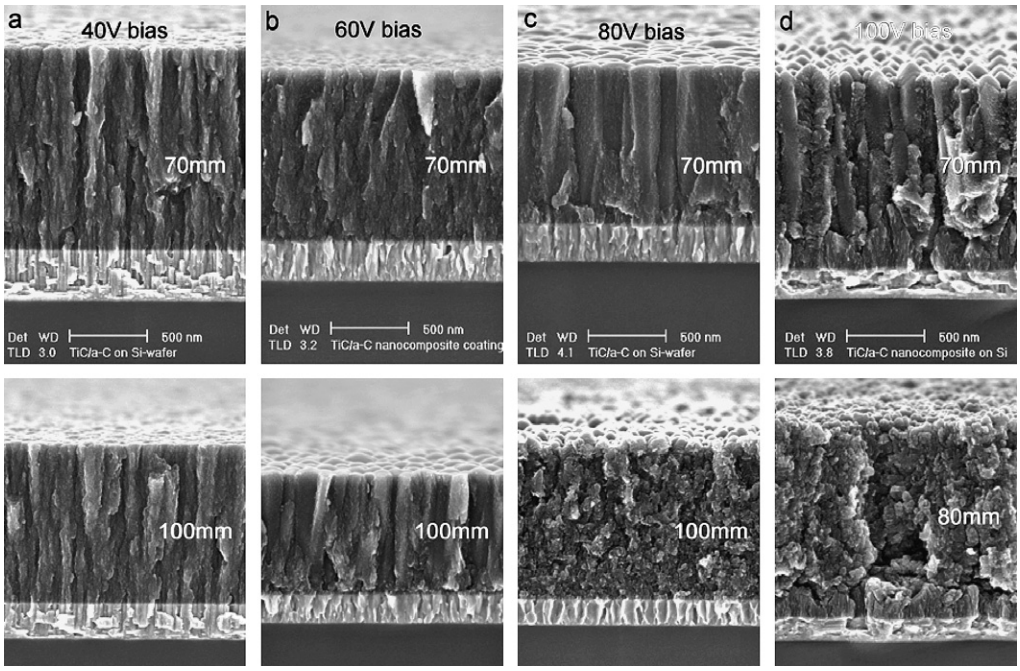

Fig. 1. SEM micrographs showing the fracture cross-sections of TiC/a-C nano-composite coatings deposited with DC sputtering at different substrate bias voltage (2 h deposition time): (a) 40 V, (b) 60 V, (c) 80 V and (d) 100 V with indicated distance from the targets.

The results are shown in Fig. 2. By increasing the carbon content from 82 to 94 at.%, the columnar character of the coatings does not show any essential difference, except for the fact that the coating of higher carbon content becomes slightly denser. Even the coating of pure carbon exhibits a columnar microstructure (Fig. 2c). It is apparent that the effect of increasing the carbon content is minor in restraining the columnar growth, which is rather different from the situation of reactively sputtered TiC/a-C:H nanocomposite coatings [16]. In conclusion, it is almost impossible to deposit column-free TiC/a-C coatings with DC magnetron sputtering. The only exception is the pure carbon coating deposited on the substrate that is kept stationary in front of the graphite target (Fig. 2d), where a continuous impingement of high flux ions is available. In this sense, it provides a clue as how to prohibit the columnar microstructure in TiC/a-C coatings; that is, to enhance the flux of the impinging ions, especially during the travel of substrates passing from one target to another.

3.2. Pulsed DC magnetron sputtering of TiC/a-C nanocomposite coatings

Fig. 3 shows the fracture cross-section of the TiC/a-C coatings deposited with p-DC magnetron sputtering. Switching from DC to p-DC sputtering of 100 kHz frequency does not change the columnar microstructure much, but the CBs become more widely dispersed (Fig. 3a). By increasing the frequency of sputtering DC pulses to 250 kHz and keeping all the other parameters unchanged, the coating surface becomes much smoother and the columnar feature is almost invisible. Up to 350 kHz p-DC sputtering, the deposited coating is fully column-free, with a surface (actually the growing interface) so

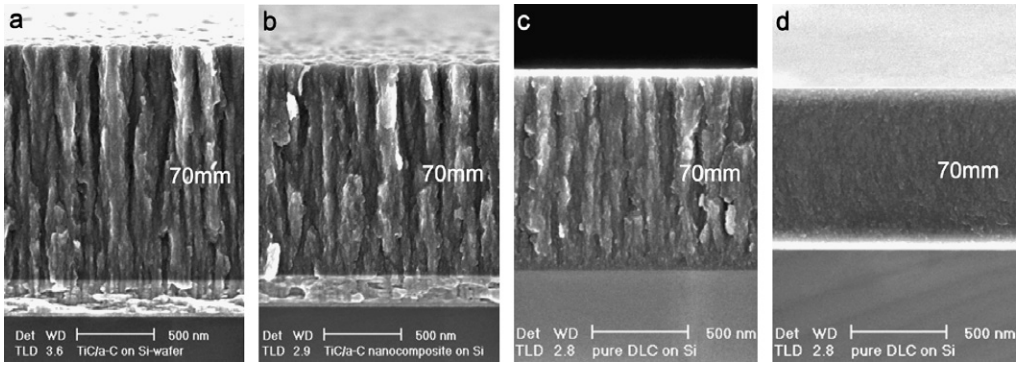

Fig. 2. SEM micrographs showing the fracture cross-sections of TiC/a-C nano-composite coatings deposited in 2 h with DC sputtering at 60 V substrate bias and of different carbon content: (a) 82 at.%, (b) 94 at.%, (c) 100 at.% and (d) 100 at.% on a stationary substrate (1 h deposition time).

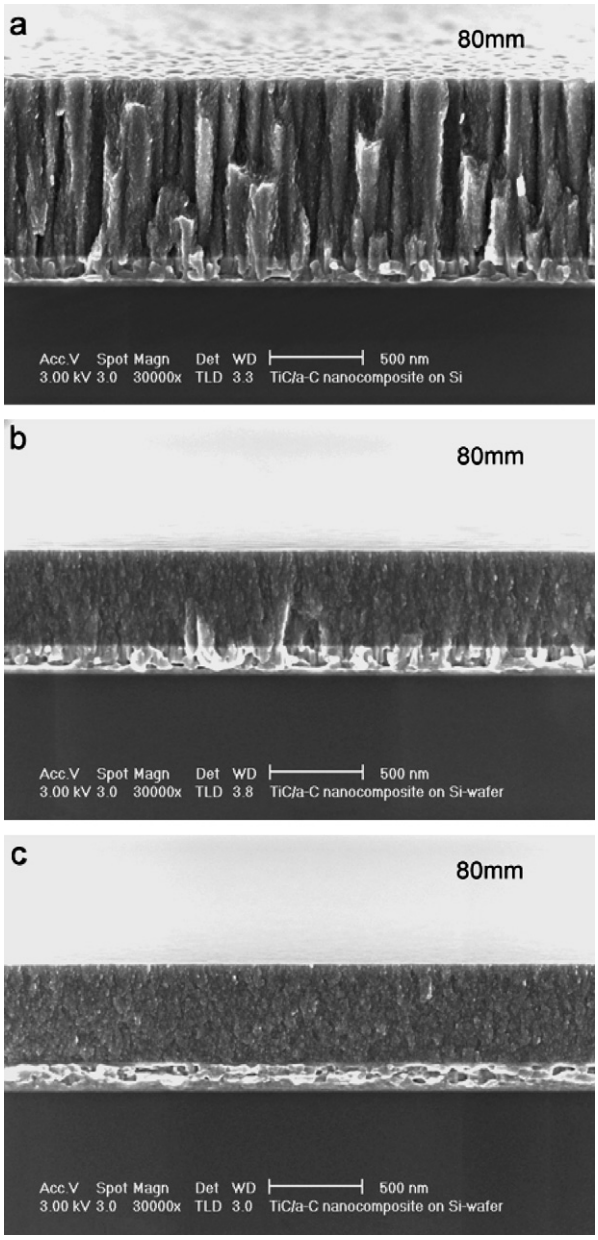

Fig. 3. SEM micrographs showing the fracture cross-sections of TiC/a-C nano-composite coatings deposited in 2 h with pulsed DC sputtering at 40 V substrate bias and different pulse frequency (50% duty cycle): (a) 100 kHz, (b) 250 kHz and (c) 350 kHz.

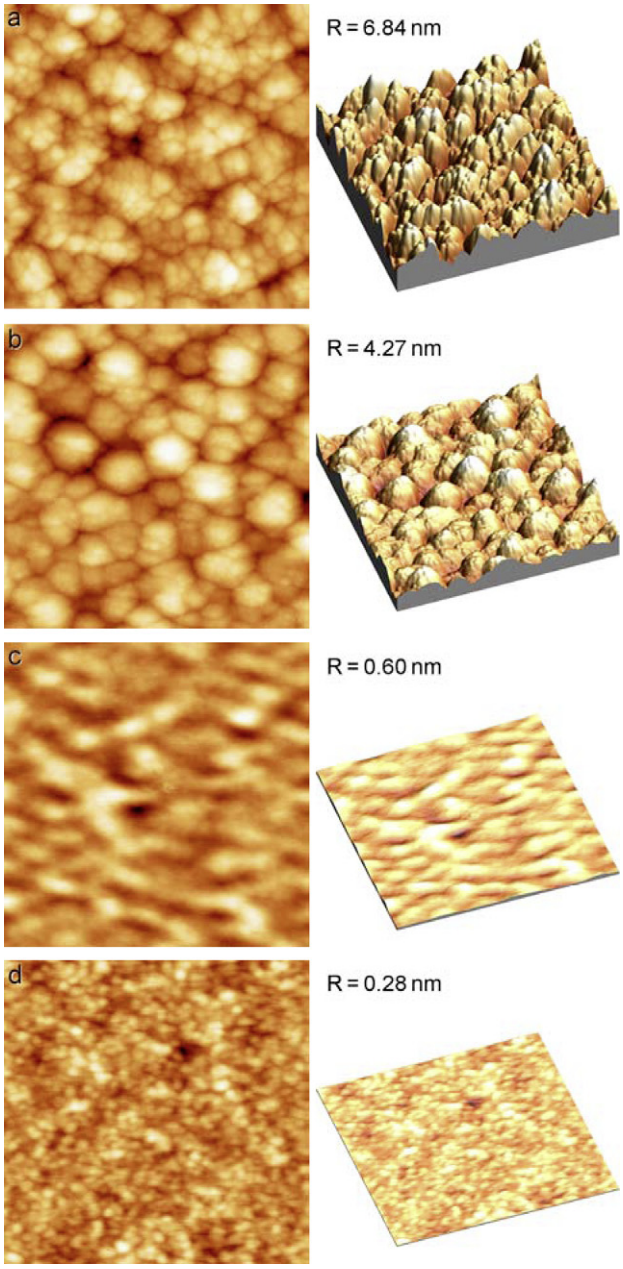

Fig. 4. AFM micrographs in dimensions of $1 \times 1\ \mu m^2$ showing the surface morphology of the TiC/a-C coatings deposited at different sputtering modes: (a) DC, (b) 100 kHz p-DC, (c) 250 kHz p-DC and (d) 350 kHz p-DC. The height amplitude of the 3D images in the right column is normalized whereas the colour codes of each image represent the corresponding maximum height ranges, respectively. The RMS roughness (R) is marked. (For interpretation of the references to colour in this figure, the reader is referred to the web version of this article.)

smooth that it hardly shows any contrast at the magnification used for scanning electron microscopic observation. The surface morphology of the coatings is therefore revealed with AFM. Switching from DC sputtering to p-DC sputtering, the surface morphology of the coatings evolves from cauliflower-like patterns to shallow domes at 100 kHz, weak ripples at 250 kHz and a flat surface with nanometer-sized bumps at 350 kHz, as shown in Fig. 4. The direct effect of this evolution is a dramatic reduction in the surface roughness of the coatings, from 7.07 ± 0.71 down to 0.29 ± 0.01 nm.

The height–height correlation function of the coating surfaces presented in Fig. 5 provides characteristic information about the surface morphology of the coatings. Here the height–height correlation function is calculated with the equation $H(r) = \langle [h(x) - h(x+r)]^2 \rangle$, where h is the height distribution function over a scanned surface and r is the lateral distance along the fast scanning direction. The angle brackets denote an average over the entire area scanned in an AFM micrograph. Assuming a self-affine scaling behavior, the height–height correlation function takes the form

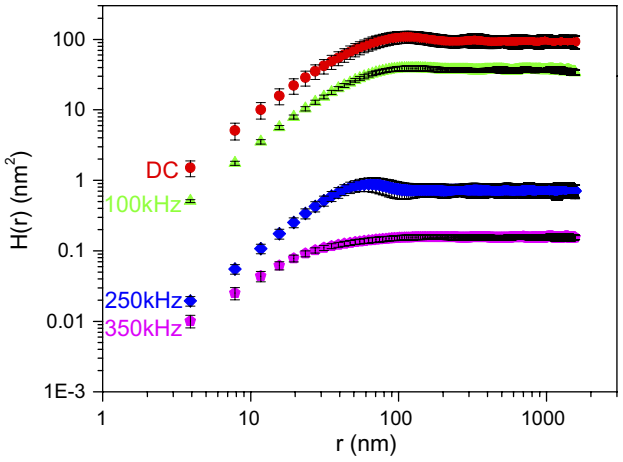

Fig. 5. Height–height correlation (H) graph of the coatings deposited at different sputtering modes.

$H(r) = 2w^2 f(r/\xi)$ with $H(r) = (mr)^{2\alpha}$ for $r \ll \xi$ and $H(r) = 2w^2$ for $r \gg \xi$ [20,21]. The lateral correlation length ξ defines the lateral distance within which the surface heights of any two points are correlated and the interface width w is the equivalent of the root mean square roughness measured by AFM. The roughness exponent α describes the undulation of a surface, such that a larger value of α corresponds to a smoother interface structure whereas a smaller α value corresponds to a locally more jagged interface morphology. The calculated values of all the correlation parameters are listed in Table 1. The dramatic decrease in lateral correlation length and interface width with increasing p-DC frequency is a direct measure of the morphological evolution and smoothening process of the growing interfaces. The average interface slope m shows a monotonic decrease from the DC sputtered coating to the coating sputtered at 350 kHz p-DC, reflecting the general smoothening trend of the growing interfaces under concurrent ion impingement. However, the interface becomes locally rougher at a nanometer scale at higher p-DC frequency, as indicated by a smaller value of α.

It should be pointed out that the restraint of a columnar microstructure with p-DC sputtering is achieved at the expense of a reduced deposition rate. The deposition rate of TiC/a-C coatings at 50% duty cycle and p-DC frequency 100, 250 and 350 kHz is 74.7%, 45.0% and 45.3%, respectively, of the deposition rate with DC sputtering. Once the p-DC frequency rises above 250 kHz, the deposition rate does not decrease any further, which is different from the situation of reactive p-DC sputtering, where a linear relationship between the net deposition rate and the pulse factor was observed [22]. One should note that the 50% duty cycle for p-DC sputtering used is the lowest allowable value of the power supplies, and also leads to lower sputtering yields. Obviously, the extent of reduction of deposition rate also depends on the sputtering yield of different kinds of targets at different frequencies and duty cycles. In addition, the coatings deposited with p-DC sputtering are denser and a measure of smaller growth rate.

Table 1
Parameters of height–height correlation function of TiC/a-C coatings deposited at different sputtering modes

Sputtering mode	α	m	w (nm)	ξ (nm)
DC	0.838	0.3317	6.867	90
100 kHz p-DC	0.856	0.1747	4.260	85
250 kHz p-DC	0.798	0.0213	0.604	50
350 kHz p-DC	0.657	0.0078	0.279	30

It is interesting to note that, under p-DC sputtering, the distance to targets suitable for coating deposition is wide enough. Measurements (not shown) reveal that the thickness of the coatings changes inversely as a function of the distance to the targets, but its negative slope is smaller than that with DC sputtering. Moreover, the coatings deposited in the distance range of 70–100 mm all exhibit dense and column-free microstructures. This feature is of particular importance for industrial applications, where work-pieces of large sizes or large quantities of work-pieces need to be coated in one batch. The optimized microstructure of TiC/a-C coating deposited with p-DC magnetron sputtering is shown in Fig. 6a, where it is seen to consist of a ductile interlayer characterized by dense dimples on fracture, a fine and column-free microstructure, and a mirror-like surface of roughness 0.25 nm. Cross-sectional TEM observations reveal multilayered structures in both the interlayer and the top coating (Fig. 6b and c). The top coating is composed of Ti-containing sublayers and amorphous carbon (a-C) sublayers. The TiC nanocrystallites of size 4–5 nm are aligned in the Ti-containing sublayers, with an amorphous (carbon) boundary of width thinner than 1 nm. These aligned TiC nanocrystallites are separated by the a-C sublayers of about 3 nm thickness. However, the thickness of both the sublayers is readily tunable, depending on the rotational speed of the sample carousel and the sputtering current applied on the graphite and Ti targets/cathodes.

3.3. Ion energy distribution function and plasma diagnostics of p-DC sputtering

To understand the mechanism of column restraint under p-DC magnetron sputtering, ion mass/energy spectrometry was employed to diagnose the sputtering plasma, and in particular the difference in the ion energy distribution (IED) and the flux of the impinging Ar^+ ions pulled onto the growing films during p-DC sputtering of the graphite target and titanium target, respectively. Fig. 7 presents the p-DC voltage and current waveforms applied onto the graphite target at 1.25 A sputtering current. The voltage waveform of the asymmetric bipolar p-DC exhibits three characteristic periods: the pulse-on period A of negative voltage, the transition period B and the pulse-off or reverse period C (see Fig. 7a), which have been well documented in the literature [4]. The duty cycle of DC pulses is defined as the percentage of the pulse-on period to the

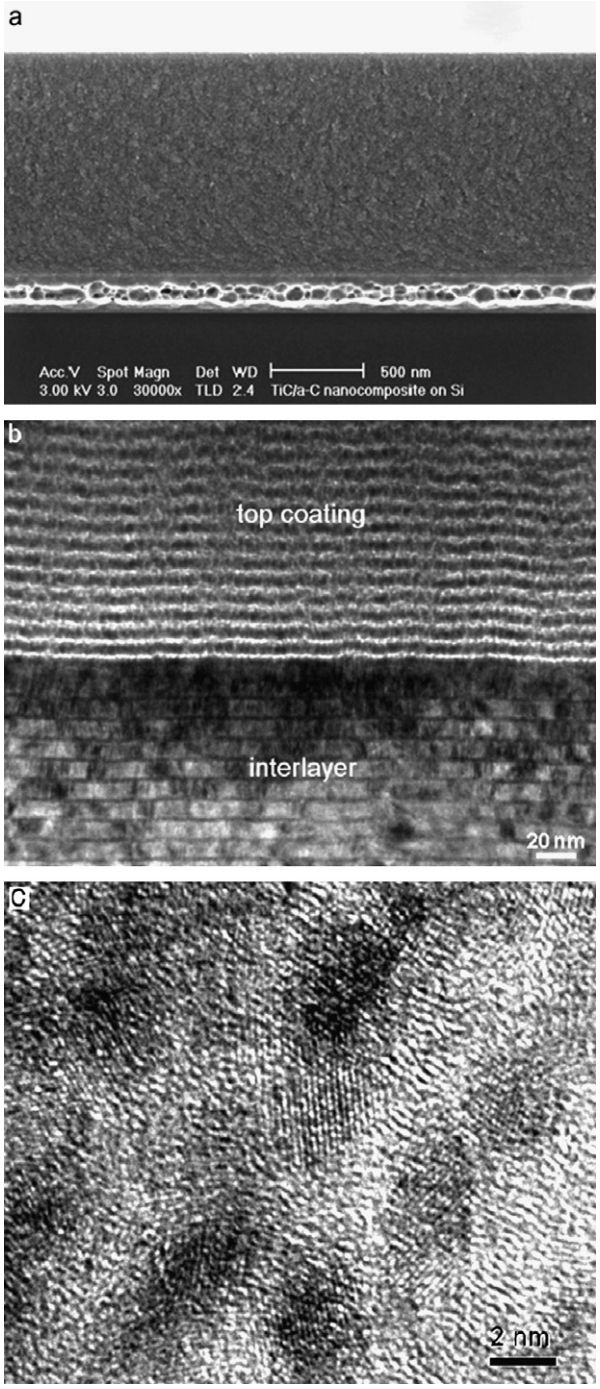

Fig. 6. (a) SEM micrograph showing the optimized microstructure of TiC/a-C nanocomposite coatings with a surface roughness of 0.25 nm; (b) XTEM overview revealing the multilayered structure of the coating and (c) HR-XTRM micrograph showing the aligned TiC nanocrystallites separated by amorphous carbon matrix sublayers of tunable thickness (the multilayers are tilted about 60° to the bottom border of the micrograph).

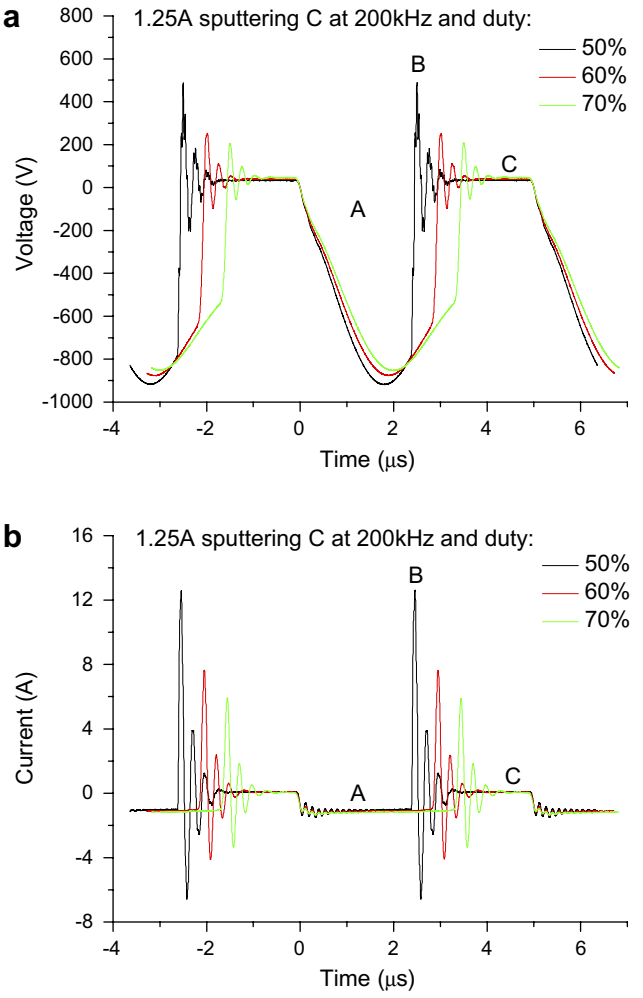

Fig. 7. Waveforms of 1.25 A p-DC sputtering graphite target at 200 kHz and different duty cycles: (a) voltage and (b) current.

whole pulse cycle. The significant features of the asymmetric bipolar p-DC power supplies used in this research include the overshoot peak of high positive voltage (around 500 V in this case) in the transition period B and the adjacent oscillating peaks as well as the low positive voltage remaining during the reverse period C. During this transition and onset of the reverse period, correspondingly, the current waveform possesses several current peaks of amplitude strongly depending on the duty cycles used (Fig. 7b). For instance, the current peaks at 50% duty cycle are of 13, 6.5, 4, 1.5 A, etc., and the strongest peak is one order of magnitude higher than the nominal current (1.25 A).

The time-averaged energy distribution and the flux of the impinging Ar^+ ions during sputtering graphite are shown in Fig. 8. The IED curves of the impinging Ar^+ ions under p-DC magnetron sputtering present three distinct populations of the ions that reflect the target voltage waveforms. That is to say, impingements of Ar^+ ions of low energy (<20 eV, peak A in Fig. 8a) occur during the pulse-on period; this is supported by the fact that DC magnetron sputtering produces only the low energy ions of the same category. The ions of intermediate energy (20–50 eV, peak C in Fig. 8a) are generated during the reverse period, which is evident because the population of this category of ions diminishes with decreasing reverse period (i.e. increasing the duty cycle at a chosen p-DC frequency), as shown in Fig. 8b. Those ions of high energy extending over

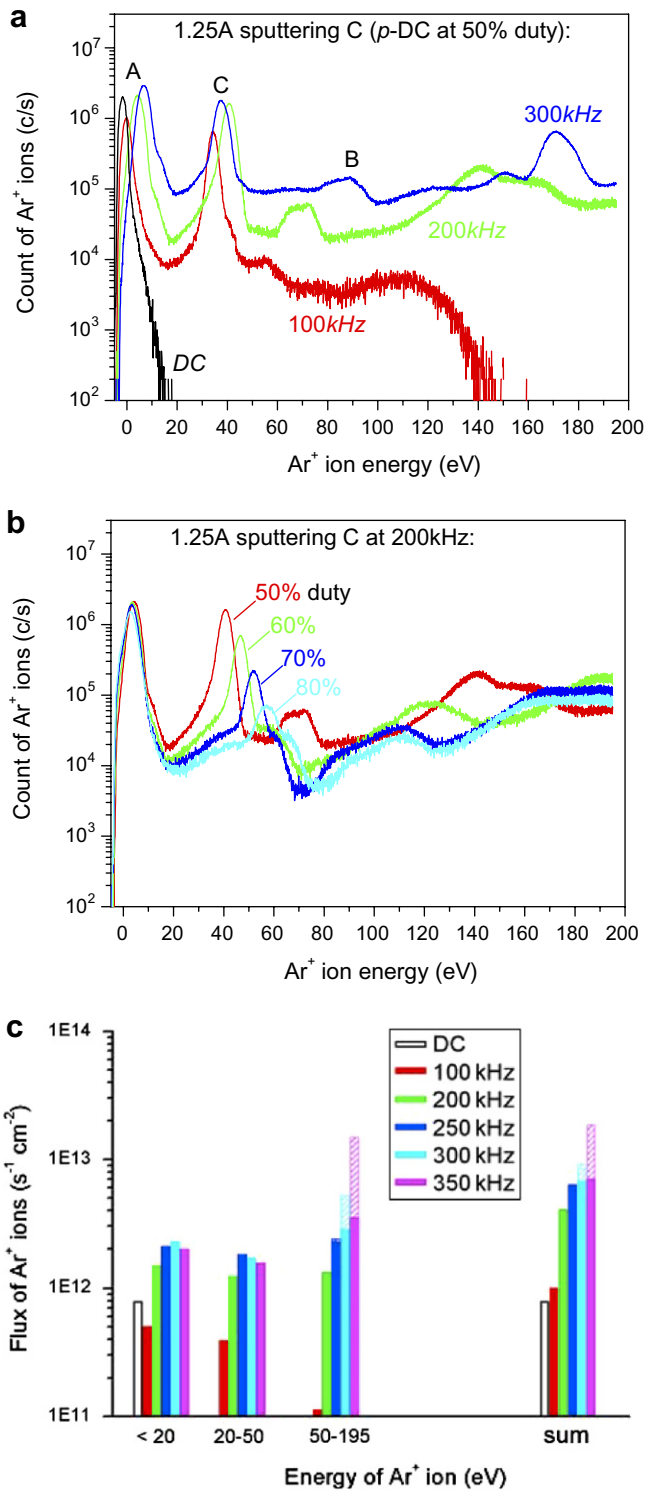

Fig. 8. Energy distribution of impinging Ar^+ ions incident on the growing coatings during sputtering graphite target with DC or pulsed DC of different frequencies (a) and at 200 kHz of different duty cycles (b); (c) flux of impinging Ar^+ ions in three energy ranges as well as the sum at different p-DC frequencies of 50% duty cycle (substrate grounded). The hatched part of the columns is the missed flux due to the cutoff of the energy spectrometer beyond 195 eV, estimated according to the fraction of the transition period in a pulse of different frequencies.

200 eV are created during the transition period, accelerated by the high potential fall (positive voltage peaks) towards the grounded substrate. Because of the detection limit of the energy spectrometer, the energy distribution function curves at a p-DC frequency above 200 kHz are partly cut off beyond 195 eV. It is clear that the energy distribution function of the impinging Ar^+ ions is governed by the sputtering mode, p-DC frequency and duty cycle, as already known. Similar results of impinging Ar^+ ion energy distribution as a function of p-DC frequency are observed during sputtering of the Ti target, as shown in Fig. 9. In comparison with sputtering graphite targets, the voltage in the pulse-on period is lower, about 500 V in sputtering Ti vs. 900 V in sputtering C. The overshoot peaks of voltage and current measured during sputtering titanium are much lower – only about one-third of the amplitudes of those peaks observed in the former case. As a result, the energy spread of the high energy Ar^+ ions is reduced and most of the energy distribution function curves fall into the measurement range of the energy spectrometer

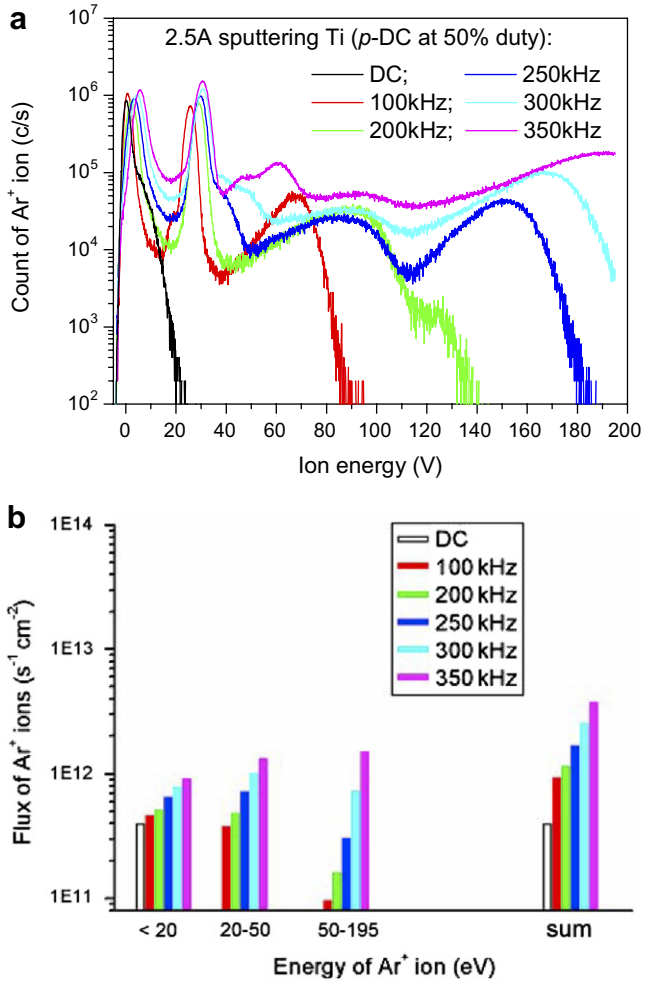

Fig. 9. (a) Energy distribution of impinging Ar^+ ions incident on the growing coatings during sputtering Ti target with DC or pulsed DC of different frequencies and (b) flux of the Ar^+ ions in three energy ranges as well as the sum at different p-DC frequencies (substrate grounded).

(Fig. 9a). This leads to a lower ion flux at each p-DC frequency (Fig. 9b), even though the sputtering current of 2.5 A is doubled on the Ti target of the same size.

The key parameters of concurrent ion impingement that control the growth behavior and microstructure of the coatings are the flux of the impinging ions and the energy delivered. As shown in Fig. 8c, the flux of the total impinging Ar^+ ions in the low frequency p-DC sputtering mode (e.g. 100 kHz) is comparable to that under DC magnetron sputtering. However, the total ions flux increases dramatically when the frequency is increased beyond 100 kHz. One should keep in mind that the total ions flux measured during sputtering C at a frequency above 200 kHz is slightly lower than the real value, due to the cutoff of the measurement of the high energy ions beyond 195 eV (Fig. 8a and b). For better comparison, the missed flux of high energy ions are estimated according to the fraction of the transition period in a pulse of different frequencies (see Fig. 8c). It is clear that the flux of total impinging ions may differ by one order of magnitude between DC magnetron sputtering and p-DC magnetron sputtering at high frequencies. Similar results are also observed during p-DC sputtering of titanium target (see Fig. 9b). In particular, the impinging ions in the intermediate and high energy bands become more and more dominant with increasing p-DC frequency, delivering a much higher energy for impingement on the growing interface of deposited coatings. To confirm this point, the product of the time-averaged ion count in each energy bin and the energy scale under the IED curves in Figs. 8a and 9a have been integrated over the measured energy range and the results are shown as energy flux in Fig. 10. It is clear that the energy flux of impinging Ar^+ ions under high-frequency p-DC sputtering is two orders of magnitude larger than that delivered with DC sputtering. Due to the different electrical conductivity and sputtering behavior of the different target materials, in particular the p-DC sputtering graphite target delivers even higher energy flux of impinging ions than sputtering titanium target (e.g. 1.26×10^{15} vs. 2.69×10^{14} eV s^{-1} cm^{-2} at 350 kHz), though the nominal sputtering current is only half of the latter case (1.25 vs. 2.5 A). However, the energy flux drops significantly at low p-DC frequencies, e.g. at 100 kHz or lower.

It is noteworthy that, in comparison with the high flux of impinging Ar^+ ions, the flux of sputtered species ions is rather low even under p-DC sputtering. As shown in Fig. 11a, the energy distribution of Ti^+ ion is very similar to the IED curves of Ar^+ ions presented in Fig. 9a, but the counts are nearly two orders of magnitude lower in all the energy bins. Although three groups of C^+ ions are recognized in the IED curves, as shown in Fig. 11b, the low energy C^+ ions dominate and their counts are three orders of magnitude lower than that of the Ar^+ ions at all the p-DC frequencies. The total ions flux and flux ratio of the sputtered species ions to the impinging Ar^+ ions are listed in Table 2. Even though the Ti^+ ion flux increases with p-DC frequency, its part in the total flux of ions

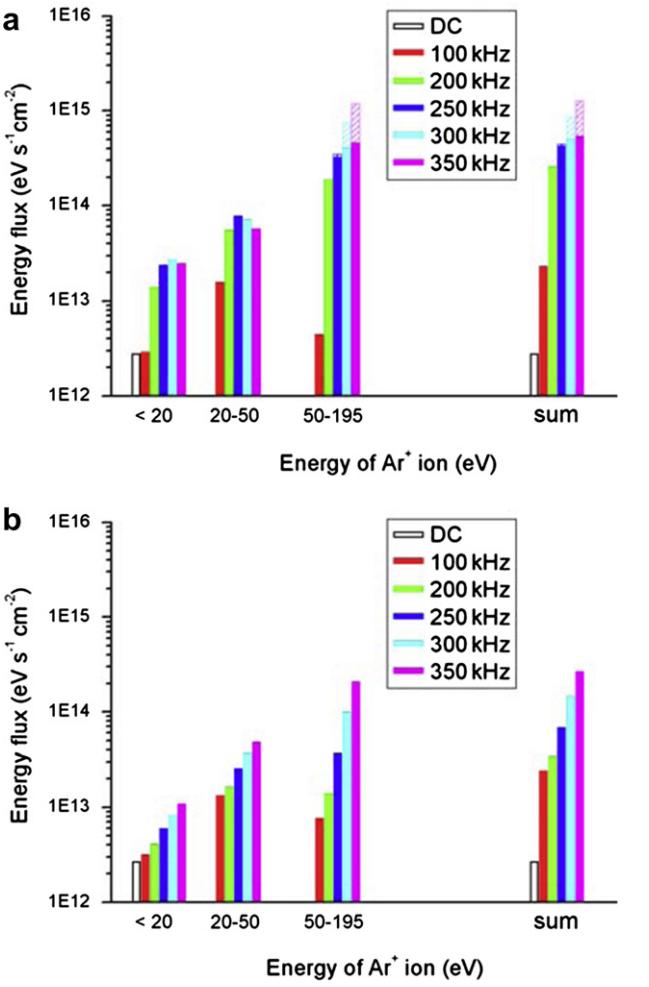

Fig. 10. Energy flux delivered to the growing interface by impinging Ar^+ ions: (a) during sputtering C with 1.25 A current and (b) during sputtering Ti with 2.5 A current DC or p-DC at different frequencies. The hatched part of the columns is the missed flux due to cutoff of the high energy ions beyond the limit of the energy spectrometer.

drawn to the growing interface is only several percent. Yet the C^+ ion flux is less than one percent. This observation is different from the results of reactive sputtering Al and Cr reported in Ref. [13], where the total flux of species ions is at least comparable to that of the impinging Ar^+ ions.

Besides the enhancement of the flux and energy distribution of impinging ions, another significant feature of p-DC magnetron sputtering is the expansion of the plasma. Fig. 12 compares the confinement of the plasma torch incident onto the substrate with different sputtering modes and frequencies. Under DC sputtering, the dense plasma torch confined in front of the target can cover only the central part of the substrate (Fig. 12a). In contrast, the plasma torch at 100 kHz p-DC sputtering covers nearly the whole substrate, but with a large intensity difference from the center to the outer fringe (Fig. 12b). Up to 250 kHz, the plasma torch gets much denser and homogeneously covers the entire substrate (Fig. 12d). It even expands to the

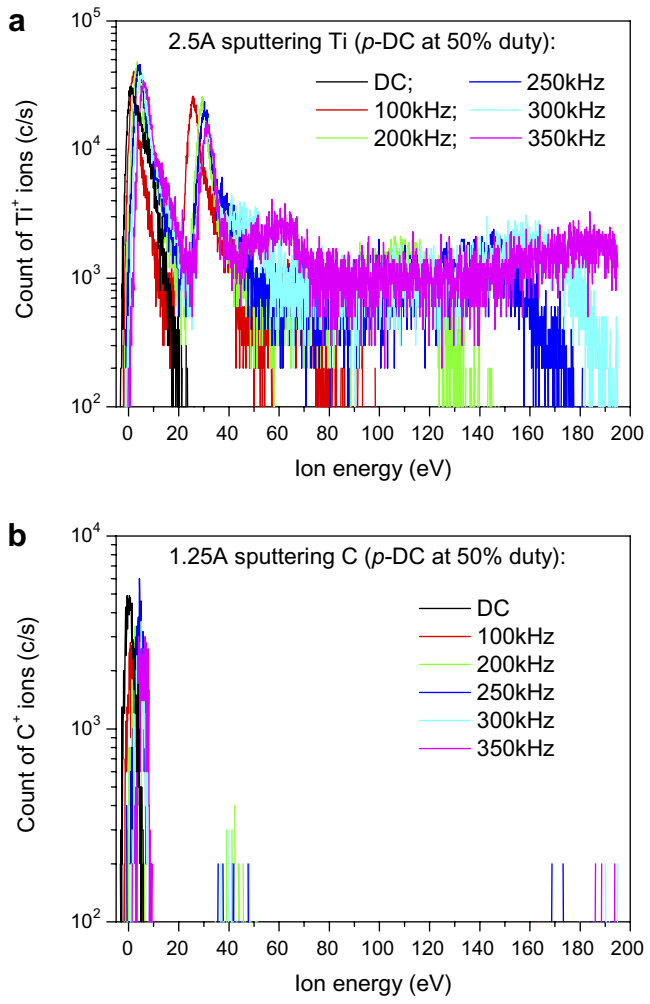

Fig. 11. Ion energy distribution of Ti^+ ions (a) and C^+ ions (b) delivered onto the growing films under DC sputtering or p-DC sputtering of different frequencies.

surrounding area, but the intensity is still very low. At the highest frequency, 350 kHz, the extensive plasma not only covers the entire substrate but also fills in the whole chamber (Fig. 12f). It is this expanded plasma that keeps the growing coating under intensive and, in particular, continuous impingement when passing from one target to another in a closed-field configuration of a multi-target sputtering system.

4. Discussions

In a so-called closed-field unbalanced magnetron sputtering system, such as the Teer UDP 400/4 rig used in this work, targets stand vertically along the circular chamber wall while the substrates mounted on the sample carousel rotate around the central axis of the chamber (single spindle rotation) and pass the targets one by one at a chosen distance. For reactive sputtering, the decomposition of the reactive gases occurs in the plasma everywhere inside the chamber and provides some of the species for deposition that continuously reach the growing film from all angles and at any position, besides the sputtered atoms from the targets. Even in non-reactive sputtering with a co-planar configuration of magnetrons facing towards the same area or a substrate, such a continuous landing of different kinds of depositing atoms can be readily realized as well. Therefore, there is less challenge in controlling the microstructure of DLC-based composite coatings in these two cases. Different from the preceding situation, during non-reactive sputtering with a closed-field unbalanced magnetron sputtering system the landing of sputtered atoms is interrupted in-between the targets, and ion impingement may fluctuate to a large extent. This may readily lead to either multilayered coatings due to composition variation or undesired microstructures because of unstable ion impingement. This work focuses on the influence of pulsed magnetron sputtering on the depositing process and consequently on the microstructure evolution of the deposited coatings, rather than on the sputtering process itself. It is clearly demonstrated that pulsing the unbalanced magnetrons may dramatically change the property of the plasma and consequently enhance the intensity of the concurrent ion impingement on the growing interface of deposited coatings, in comparison with DC sputtering. As a result, a desired microstructure may be tailored to achieve the superior performances of advanced coatings.

4.1. Influence of pulsing magnetrons on plasma properties

The enhanced total flux of impinging Ar^+ ions onto the growing film is a typical attribute of the p-DC magnetron operation, as has been reported previously [4]. The time-resolved Langmuir probe measurements conducted concurrently with the energy-resolved mass spectroscopy

Table 2
Ion flux and flux ratio of sputtered ions to impinging Ar^+ ions when sputtering different targets

Sputtering condition		Flux of ions (s^{-1} cm^{-2})	DC sputtering	p-DC sputtering (kHz)				
Target	Current (A)			100	200	250	300	350
Ti	2.5	$Ti^+ \times 10^{10}$	2.60	4.12	5.66	6.28	6.34	6.58
		$Ar^+ \times 10^{12}$	0.40	0.94	1.16	1.68	2.54	3.75
		Ti^+/Ar^+ (%)	6.50	4.38	4.88	3.74	2.50	1.75
C	1.25	$C^+ \times 10^9$	2.29	1.18	0.96	1.82	1.26	1.21
		$Ar^+ \times 10^{12}$	0.79	1.01	4.06	6.30	9.18	18.46
		C^+/Ar^+ (%)	0.290	0.117	0.024	0.029	0.014	0.007

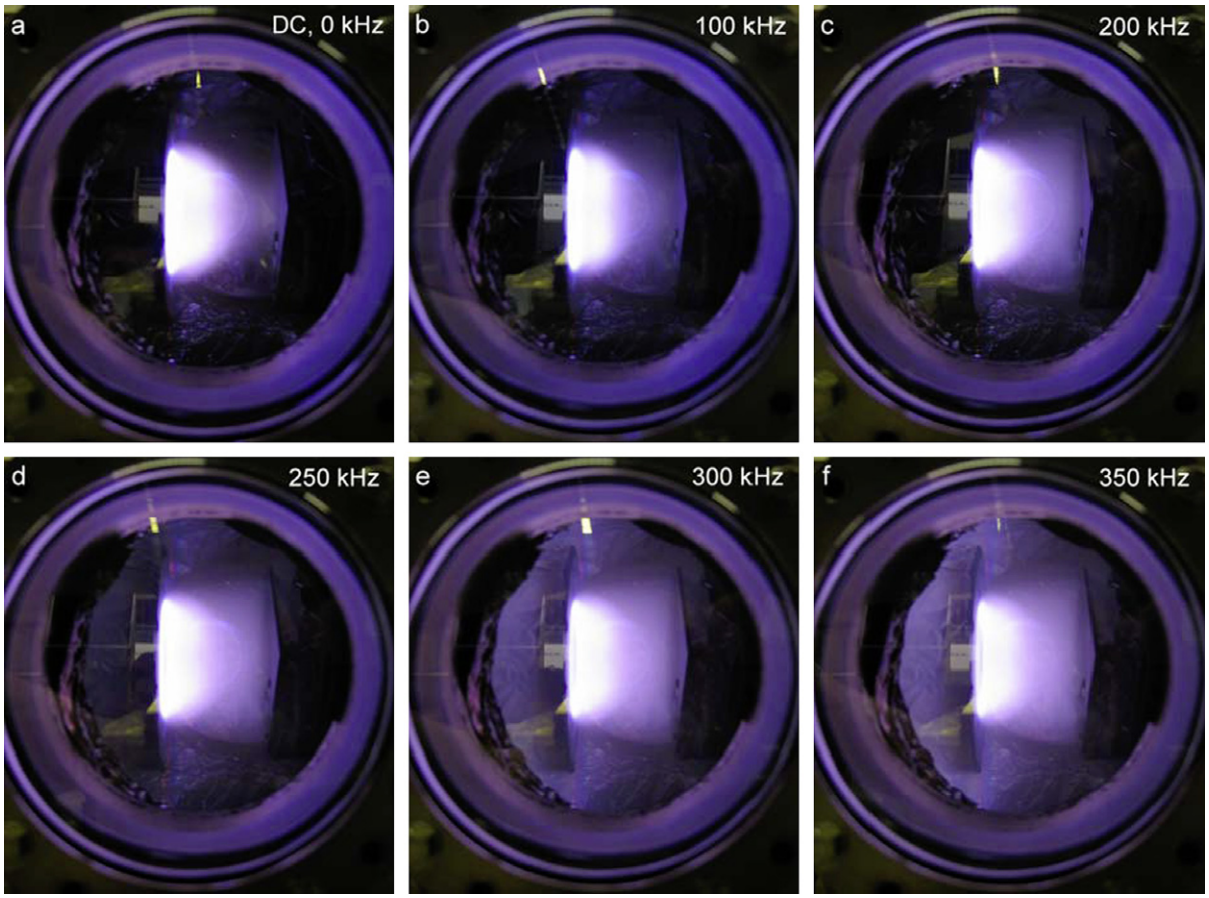

Fig. 12. Photos showing the shape and density of the plasma torch during sputtering graphite target (1.25 A and 60% duty cycle for p-DC), incident at the rectangular grounded substrate positioned to the right of viewport at 100 mm distance from the target. A much denser and extended plasma is obtained at higher frequency pulsed DC sputtering, compared with DC sputtering.

measurements revealed an approximately 30% increase in the average plasma density whilst operating at 100 kHz [23]. Therefore, the enhanced total ion flux measured in Figs. 8c and 9b can be ascribed to the higher average plasma density under p-DC sputtering. In view of this, p-DC discharge is able to transform more electrical energy into the increase of average plasma density and electron temperature than DC discharge even if the average power delivered to both of the discharges is the same. In other words, p-DC discharge more efficiently transfers plasma energy to the growing thin film. The Ar^+ ion energy distribution spectra clearly demonstrate that the ion counts in the high energy bins are lower than those in the low energy bins. However, due to the wide energy spread, the total flux of the high energy ions delivered in the period B increases with increasing pulse frequency and becomes comparable to the flux of those low energy ions delivered during the period A and C at high pulse frequencies (see Figs. 8c and 9b).

In the pulsing regime of the asymmetric bipolar p-DC power supplies, the duration of the pulse transition period B is a system constant of approximately 200 ns and is independent of the pulse frequency and duty cycle. As the pulse frequency increases, the proportion of the transition period B in the pulse cycle becomes greater and the overshoot voltage increases. Therefore, its contribution to the delivery of impinging Ar^+ ions of high energy must increase as well. Furthermore, cathode current waveforms reveal that the discharge electron current during the cathode overshoot period B noticeably increases with pulse frequency (not shown here), as well as reversing the flow direction. The lack of bulk electrons during this period causes the plasma sheath adjacent to the grounded substrate/orifice to expand more with increasing pulse frequency. As a result, the volume of ion sheath in the front of the orifice increases with pulse frequency and consequently the number of ions attracted onto the growing film or into the energy spectrometer during the pulse transition period B increases as shown in Figs. 8c and 9b. These effects result in a much higher total energy flux density on the substrate, as has been observed during an independent measurement by using a calorimeter probe placed at the substrate position [24].

The enhanced flux and impinging energy of argon ions on the growing films and the grounded walls bring about an increased generation of secondary electrons. These electrons are accelerated back to the plasma, and kinetic energy acquired through the plasma sheath enables them

to excite or ionize atoms and molecules of working gas. As a result of this process, glow discharge is observed not only from the volume between the target and substrate but also in the whole chamber. This effect is well discernible, particularly at 300 and 350 kHz, as illustrated in Fig. 12.

From our measurements, it follows that Ar^+ ion energy flux on the substrate depends strongly on the shape and magnitude of the cathode voltage overshoot (pulse transition period B) and also on the material of which the target is made. Differences between the magnitudes of the ionization potential, sputtering yield and secondary electron emission coefficients of carbon and titanium can affect the plasma parameters, cathode voltage and current waveforms. These parameters are then crucial in determining the plasma intensity and ion energy flux onto the growing film.

4.2. Effects of interface smoothening

The restraint of the columnar microstructure is attributed to the interface smoothening induced by intensive concurrent ion impingement. In the surface growth of film deposition, the competition between interface roughening and smoothening essentially determines the microstructure and consequently the properties of the deposited film [25]. Interface shadowing, dynamic scaling and kinetic roughening are the primary mechanisms of surface roughening [26–28]. On the other hand, surface diffusion [29,30], re-emission [31], sputter redeposition [32] and surface relaxation at high homologous temperatures [33] are the proposed mechanisms to smooth out the growing interface. Unlike the first two smoothening mechanisms, which are local events of individual adatoms, sputter redeposition and surface relaxation are collective activities. Since no intentional heating has been used during coating depositions and the temperature of the substrates is in the range of 150–170 °C, surface relaxation is not a concern in this work. Instead, sputter redeposition is considered as the main acting mechanism under the deposition conditions employed, which is better termed "adatom transfer" induced by concurrent ion impingement so as to avoid any confusion with the primary sputtering process on the targets. Although Ar^+ ions of 5 keV were used to etch the graphite surface when the mechanism was originally proposed [32], the "adatom transfer" mechanism is applicable here since the p-DC sputtering process itself employs Ar^+ ions of hundreds eV energy (see Fig. 7a). The maximum energy of concurrent impinging Ar^+ ions delivered in the pulse transition period B is above 200 eV, which is high enough to transfer adatoms, even if it is not high enough for resputtering the adatoms away.

As reported in Figs. 3, 8c and 9b, pulsed DC sputtering has a double effect on the deposition process: reduced flux of depositing atoms and increased flux of impinging ions with a much extended range of energy distribution. This implies a much higher energy per depositing atom delivered to the growing interface for reconstruction at higher pulse frequencies, as confirmed in Fig. 10. The physical mechanism of adatom transfer is sketched in Fig. 13. Consider

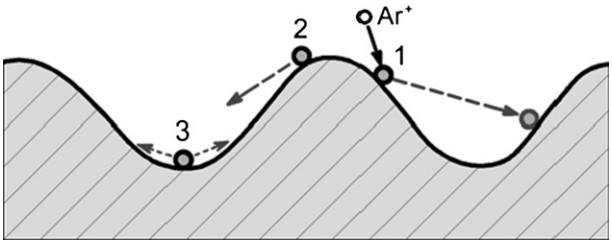

Fig. 13. Sketch showing adatom transfer by impinging Ar^+ ions: from the crest to the valleys (1 and 2) and inside the same valley (3).

a $1+1$ (including time) dimension case: every point on the growing interface is assumed to receive impinging ions from all angles of incidence that are not shadowed by other neighboring surface features [31,34]. However, the crest of the prominent peaks receives more impinging ions than the valleys because the exposed angles on a convex surface are larger than those on a concave surface. This is equivalent to the case of shadowing growth but with an opposite effect of erosion. That is to say, shadowing always leads to interface smoothening during erosion. The impinging ions may transfer the adatoms if the ion energy is in an appropriate range. What is essential in this case is that most of the re-sputtered adatoms from the crests redeposit onto the valleys, owing to the morphological confinement. In contrast, the re-sputtered adatoms from the valley can only redeposit onto the foot of the peaks, namely still inside the valleys (Fig. 13). Apparently, such preferential etching at the crests competes with shadowing growth in a metastable manner. As the ion flux and especially the energy flux increase significantly with increasing p-DC frequency, preferential etching of the prominent peaks surpasses shadowing growth so that the growing interface becomes smoother. It thus explains why the high energy ions are necessary and more efficient for interface smoothening and restraint of the columnar growth, which are available only at higher p-DC frequencies ($\geqslant$250 kHz). The preliminary results of molecular dynamics simulation confirms this phenomenon and will be published elsewhere.

Another possible interface smoothening mechanism involving concurrent ion impingement is the thermal spike model [35]. The basic idea of this model is that the energy of incoming energetic particles dissipates locally as heat in a so-called thermal spike of picoseconds that leads to local surface melting and thus flattens the interface due to minimization of surface energy. Different from the original deposition process (filtered arc deposition) of the proposed model, where the energy carriers are depositing C^+ ions rather than impinging Ar^+ ions, the model is less applicable to the current sputtering process in which the interface smoothening is resulted directly from the enhanced intensity of concurrent ion impingement with pulsing the magnetrons. In the case of filtered arc deposition, the energy delivered to the growing interface is always proportional to the depositing rate or the probability of receiving the energized particles at an interface position. This implies a relatively homogeneous smoothening effect along the

interface rather than preferential etching, whether on the crests or in the valleys. In particular, the local interface should become smoother with increasing energy flux or increasing heat of the thermal spikes and thus the area of local melting. That is not the case reported here, as seen in the evolution of the roughness exponent α in Table 1 and Figs. 4 and 5.

4.3. Control of nanostructure

In nanocomposite coatings composed of hard nanograins and a compliant matrix, two different designs have been recently put into practice in thin film applications, namely superhard and super-tough nanocomposite coatings [36]. The concept of superhard nanocomposite coatings lies in the suppression of dislocation operation by using small (3–5 nm) grains and inducing grain incoherence strains with a <1 nm thin matrix for grain separation. On the other hand, nanocomposite coatings generate a high density of interphase interfaces that assist in crack deflection and termination of crack propagation. The introduction of an amorphous matrix facilitates grain sliding that releases the strain energy stored. Based on these toughening mechanisms, the concept of super-tough nanocomposite coatings has been proposed such that, for supertoughness, a coating structure should consist of 10–20 nm nanocrystalline grains separated by a 2–10 nm amorphous matrix [37]. However, such a combination of large nanograins with a wide matrix separation is not favored from the viewpoint of atomic migration during deposition. Considering common deposition conditions, magnetron sputtering with a negative substrate bias not higher than 150 V but without intentional substrate heating is less likely to generate atomic displacement over a distance of several nanometers through surface diffusion or subsurface migration. Therefore many smaller nanograins, i.e. smaller than 10–20 nm, are formed in the amorphous matrix with separations that are determined by the elemental concentration. In our recent work on TiC/a-C:H nanocomposite coatings [16], the minimum size of TiC nanocrystallites observed was 2 nm. The particle size does not increase until the matrix separation diminishes with increasing Ti content to a certain limit, due to the competition between grain nucleation and grain growth. Based on these observations, a toughening mechanism of delocalizing cracks has been proposed. That is to say, by keeping the suppression of crack nucleation in an amorphous matrix, the introduction of nanoparticles may spread the localization of cracks into a delocalized state. The ductility and therefore the toughness will be enhanced provided the particle size d becomes approximately the same size as the separation.

To manipulate the size and separation of TiC nanocrystallites, one possible approach is to tailor a multilayered structure into a nanocomposite coating such that the nanocrystallite-containing sublayers are separated by the matrix sublayers of desired thickness via composition fluctuation during deposition. Through such an integrated multilayer-composite structure, the size and separation of TiC nanoparticles can be well controlled independently (Fig. 6c), which was not possible in a homogeneous nanocomposite coating. The multilayered nanocomposite coating exhibits essential enhancement in fracture toughness and it is hardly possible to induce radial cracks via nanoindentation with a cube-corner diamond indenter even if the indenter has penetrated through the entire coating thickness. Its tribological performance is also superior and comparable with advanced TiC/a-C:H nanocomposite coatings [38]. Detailed characterization of the nanostructure and properties of the optimized TiC/a-C nanocomposite coating will be published elsewhere.

5. Conclusions

Pulsed DC magnetron sputtering can control the flux and energy distribution of impinging Ar^+ ions over a very broad range compared with DC sputtering, which delivers only low energy Ar^+ ions and a much smaller flux. The most striking result observed is in the capability of microstructural control of TiC/a-C nanocomposite coatings with pulsed DC magnetron sputtering at high frequencies ($\geqslant$250 kHz), especially constraining the formation of columnar microstructure. With increasing pulse frequency, the nanocomposite coatings exhibit evolutions in morphology of the growing interface from rough cauliflower patterns to flat interfaces composed of nano-sized bumps and in microstructure from strongly columnar to columnar-free, and become fully dense. Physical arguments are proposed to understand this interface evolution. The concurrent ion impingement etches prominent interface peaks because exposed crests receive more flux of impinging ions that preferentially transfer adatoms to the valleys.

Acknowledgements

This research was carried out under project number MC7.06246 in the framework of the Strategic Research programme of the Netherlands Institute for Metals Research (NIMR). The authors acknowledge financial support from the NIMR and the Foundation for Fundamental Research on Matter (FOM-Utrecht), The Netherlands. G. Clarke, from the Surface Engineering Group, Department of Biology, Chemistry and Health Science, Manchester Metropolitan University, UK, is acknowledged for his assistance in the experiment of plasma diagnostics with ion mass/energy spectrometer. Dr. D. Vainshtein, from Department of Applied Physics, the Netherlands Institute for Metals Research, is gratefully acknowledged for valuable discussions.

References

[1] Schiller S, Goedicke K, Reschke J, Kirchhoff V, Schneider S, Milde F. Surf Coat Technol 1993;61:331.
[2] Kelly PJ, Arnell RD. Vacuum 2000;56:159.

[3] Arnell RD, Kelly PJ, Bradley JW. Surf Coat Technol 2004;188:158.
[4] Bradley JW, Bäcker H, Aranda-Gonzalvo Y, Kelly PJ, Arnell RD. Plasma Source Sci Technol 2002;11:165.
[5] Bartzsch H, Frach P, Goedicke K. Surf Coat Technol 2000;132:244.
[6] Kelly PJ, Arnell RD. J Vac Sci Technol 1999;A17:945.
[7] Audronis M, Kelly PJ, Leyland A, Mattews A. Thin Solid Films 2006;515:1511.
[8] Onifade AA, Kelly PJ. Thin Solid Films 2006;494:8.
[9] Bradley JW, Bäcker H, Kelly PJ, Arnell RD. Surf Coat Technol 2000;135:221.
[10] Bradley JW, Backer H, Kelly PJ, Arnell RD. Surf Coat Technol 2001;142–144:337.
[11] Moiseev T, Cameron DC. Surf Coat Technol 2006;200:5306.
[12] Budtz-Jørgensen CV, Bøttiger J, Kringhøj P. Surf Coat Technol 2001;137:104.
[13] Lin J, Moore JJ, Mishra B, Sproul WD, Rees JA. Surf Coat Technol 2007;201:4640.
[14] Anton JM, Mishra B, Moore JJ, Moore JJ, Rees JA, Sproul WD. Surf Coat Technol 2006;201:4131.
[15] Kelly PJ, Beevers CF, Henderson PS, Arnell RD, Bradley JW, Bäcker H. Surf Coat Technol 2003;174–175:795.
[16] Pei YT, Galvan D, De Hosson JTM. Acta Mater 2005;53: 4505.
[17] Galvan D, Pei YT, De Hosson JTM. Surf Coat Technol 2006;200:6718.
[18] De Hosson JTM, Pei YT, Galvan D. Surfaces and interfaces in nanostructured materials II. In: Mukhopadhyay SM, Dahotre NB, Seal S, Agarwal A, editors. TMS 2006. p. 59–68.
[19] Horcas I, Fernández R, Gómez-Rodríguez JM, Colchero J, Gómez-Herrero J, Baro AM. Rev Sci Instrum 2007;78:013705.
[20] Zhao YP, Wang GC, Lu TM. Characterization of amorphous and crystalline rough surface: principles and applications. London: Academic Press; 2001.
[21] Wouters O, Vellinga WP, Van Tijum R, De Hosson JTM. Acta Mater 2005;53:4043.
[22] Kelly PJ, Onifade AA, Zhou Y, Clarke GCB, Audronis M, Bradley JW. Plasma Process Polym 2007;4:246.
[23] Bradley JW, Bäcker H, Kelly PJ, Arnell RD. Surf Coat Technol 2001;135:221.
[24] Čada M, Bradley JW, Clarke GCB, Kelly PJ. J Appl Phys 2007;102:063301.
[25] Bales GS, Bruinsma R, Eklund EA, Karunasiri RPU, Rudnick J, Zangwill A. Science 1990;249:264.
[26] Reinker B, Moske M, Samwer K. Phys Rev B 1997;56:9887.
[27] Pelliccione M, Karabacak T, Gaire C, Wang GC, Lu TM. Phys Rev B 2006;74:125420.
[28] Tong WM, Williams RS. Annu Rev Phys Chem 1994;45:401.
[29] Tamborenea PI, Das Sarma S. Phys Rev E 1993;48:2575.
[30] Bray KR, Parsons GN. Phys Rev B 2001;65:035311.
[31] Drotar JT, Zhao YP, Lu TM, Wang GC. Phys Rev B 2000;61:3012.
[32] Eklund EA, Snyder EJ, Williams RS. Surf Sci 1993;285:157.
[33] Erlebacher J, Aziz MJ, Chason E. Phys Rev Lett 2000;84:5800.
[34] Bales GS, Zangwill A. J Vac Sci Technol 1991;A9:145.
[35] Casiraghi C, Ferrari AC, Ohr R, Flewitt AJ, Chu DP, Robertson J. Phys Rev Lett 2003;91:226104.
[36] Cavaleiro A, De Hosson JTM. Nanostructured coatings. New York: Springer-Verlag; 2006.
[37] Voevodin AA, Zabinski JS. Thin Solid Films 2000;370:223.
[38] Pei YT, Huizenga P, Galvan D, De Hosson JTM. J Appl Phys 2006;100:114309.